



Cite this: *Soft Matter*, 2018, 14, 9819

# Geometric stabilisation of topological defects on micro-helices and grooved rods in nematic liquid crystals†

Maryam Nikkhou \*<sup>a</sup> and Igor Muševič<sup>bc</sup>

We demonstrate how the geometric shape of a rod in a nematic liquid crystal can stabilise a large number of oppositely charged topological defects. A rod is of the same shape as a sphere, both having genus  $g = 0$ , which means that the sum of all topological charges of defects on a rod has to be  $-1$  according to the Gauss–Bonnet theorem. If the rod is straight, it usually shows only one hyperbolic hedgehog or a Saturn ring defect with negative unit charge. Multiple unit charges can be stabilised either by friction or large length, which screens the pair-interaction of unit charges. Here we show that the curved shape of helical colloids or the grooved surface of a straight rod create energy barriers between neighbouring defects and prevent their annihilation. The experiments also clearly support the Gauss–Bonnet theorem and show that topological defects on helices or grooved rods always appear in an odd number of unit topological charges with a total topological charge of  $-1$ .

Received 2nd August 2018,  
Accepted 13th November 2018

DOI: 10.1039/c8sm01583j

[rsc.li/soft-matter-journal](http://rsc.li/soft-matter-journal)

## 1 Introduction

Topological defects<sup>1–5</sup> are omnipresent in nature and are attracting growing interest both from fundamental and applied points of view in very different areas, ranging from cosmology to condensed-matter systems.<sup>6,10</sup> In particular, soft matter systems comprising nematic liquid crystals (NLCs) have been considered intensively to study the nature of topological defects. The NLC molecules have long-range orientational order and are characterized by the director, which is the direction of the average orientation of the molecules in a bulk of the liquid crystal (LC). Topological defects represent a region of a LC, where the order is not defined, and appear in the form of point monopoles and disclination lines or loops in the NLCs.<sup>7–12</sup>

A particle inserted into a NLC can lead to the formation of various types of topological defects, depending on the particle's shape and topology, confinement and the anchoring of the NLC molecules on the particle surface.<sup>13–20</sup> The defects can be manipulated using external field and temperature change. In particular laser tweezers can be used to manipulate very efficiently the shape and structure of topological defects.

In all the manipulation of topological defects the total topological charge is conserved, which was demonstrated in a number of articles. Colloidal particles in LCs self-assembled by topological defects can serve as complex soft-matter systems and can be controlled by laser tweezers or other external stimuli. The interrelations between the topology of particles with various genera, namely spheres,<sup>21,22</sup> rods,<sup>17,23</sup> handle-bodies,<sup>15</sup> fractals<sup>24</sup> and accompanying defects in LCs were studied, using both theoretical and experimental methods. Moreover, Yuan *et al.*<sup>25</sup> recently studied the effect of the chirality of colloidal inclusions in the form of chiral springs and helices on the colloidal self-organization in the NLC. That study was focused on the pair interactions of helical objects with tangential anchoring in the nematic elastic field, and the creation and stabilisation of topological defects on chiral springs and helices were not in the focus of that work. Senyuk *et al.*<sup>16</sup> studied topological defects on colloidal spirals, which were essentially two-dimensional objects. They found a huge variety of director configurations featuring both singular defects and smooth topological structures, which result in unusual forms of particle assembly.

We recently demonstrated full control over the creation, manipulation and annihilation of the topological charges on a long fiber immersed in a NLC.<sup>17</sup> In spite of a very simple topology of the fibre, which is of the same form as a sphere with genus  $g = 0$ , we found an amazing variety of topological defects, which could be created by light and partially stabilised in the form of point monopoles and metastable loops on a fibre. We clearly demonstrated that all the experiments of charge

<sup>a</sup> School of Physics and Astronomy, University of Leeds, Leeds LS2 9JT, UK.  
E-mail: [m.nikkhou@leeds.ac.uk](mailto:m.nikkhou@leeds.ac.uk); Tel: +44 (0)113 343 0055

<sup>b</sup> Condensed Matter Physics Department, J. Stefan Institute, Jamova 39,  
1000 Ljubljana, Slovenia

<sup>c</sup> Faculty of Mathematics and Physics, University of Ljubljana, Jadranska 19,  
1000 Ljubljana, Slovenia

† Electronic supplementary information (ESI) available. See DOI: 10.1039/c8sm01583j

creation are governed by the conservation of the total topological charge on a fibre. This means that pairs of oppositely charged monopoles or loops or zero charge loops are always created to satisfy the charge conservation requirement. Once these objects are created, they are always subject to attractive or repulsive forces of elastic origin, emanating from nearby topological defects. This means that in due time they shall be attracted and annihilated into the vacuum, which was also analysed recently in good detail.<sup>28</sup> The question remained unanswered if it is possible to stabilise pairs of oppositely charged defects at very small separation, where the elastic attractive forces are quite strong.

In this article, we study the creation and geometric stabilisation of an arbitrary number of pairs of topological defects on colloidal particles topologically equivalent to a sphere (genus  $g = 0$ ), but with complex geometrical shape. The conservation of the topological charge causes the simultaneous creation of a pair of a Saturn ring and Saturn anti-ring with opposite topological charges and winding numbers. These rings are individually inherently stable, but since they are paired and oppositely charged, they tend to attract and annihilate when their separation is less than  $\sim 40 \mu\text{m}$ . To create a series of pairs of oppositely charged topological rings on a small, rod-like colloidal particle and stabilise them within a separation of a few  $\mu\text{m}$ , we fabricated helices and grooved-cylinders, which are described and discussed in this article. We demonstrate that by controlling the number of and space between grooves in the cylinder, any odd number of topological defects with precise spatial positions can be created and stabilised. In addition, we analyse the interaction between grooved-cylinders with an arbitrary number of grooves and topological defects, which leads to the creation of novel and complex colloidal structures.

## 2 Materials and experimental methods

The micro-helices and the micro-grooved cylinders were fabricated using a direct laser writing system (Photonic Professional, Nanoscribe GmbH). The glass slides used as substrates for the fabrication of structures were cleaned with lint free wipes, isopropyl alcohol (IPA) and acetone, and sonicated in an acetone bath and IPA bath for  $2 \times 15$  min. Then for further cleaning the glasses were placed under an IPA vapor degreaser for one hour. Finally they were treated by a plasma cleaner for 15 min. A UV-sensitive polymer photoresist, IP-L 780 (Nanoscribe GmbH), was dropped on the glass slide and the selected area of the resist was exposed using a femtosecond pulsed laser at a wavelength of 780 nm and a repetition rate of 80 MHz. The laser beam is focused using a  $100\times$  oil immersion objective lens (numerical aperture  $NA = 1.4$ ). The exposed resist was polymerized only in the small focusing volume where intensities are high enough for two photon absorption, and the three-dimensional micro-structures were made. The writing process was done by moving the glass substrate relatively to the laser focus. The movement of the substrate was controlled by a motorized x-y stage for coarse displacements and a piezo stage for laser writing which has a

range of  $300 \mu\text{m}^3$ . After the writing process was completed, the sample was immersed in a SU-8 developer or IPA for 30 min, rinsed with IPA for 5 min, and blown with dry  $\text{N}_2$ . The unpolymerized photoresist was washed away and the polymerized structures remained on the glass.

Fig. 1(a) presents the SEM images of printed micro-helices and micro-grooved cylinders on a glass substrate. Each sample contains several hundreds of micro-structures. A micro-helix with 3 turns has a radius of 2 or 3  $\mu\text{m}$  and a pitch of 8 or 12  $\mu\text{m}$ . The micro-grooved cylinder was made by using 10 small cylinders stacked together with a radius of 1  $\mu\text{m}$  and a height of 2  $\mu\text{m}$ . To produce a strong homeotropic anchoring of the surrounding NLC 5CB (4-cyano-4'-pentylbiphenyl), first, the sample was exposed to a plasma gun for 10 min and then immersed gently in an aqueous solution (1 v/v%) of DMOAP silane (octadecyldimethyl-(3-trimethoxysilylpropyl)ammonium chloride, ABCR GmbH) for 5 min. Finally, the sample was washed with deionized water to remove the extra silane, blown with dry  $\text{N}_2$  and left in an oven at  $120^\circ\text{C}$  for 30 min.

The micro-structures were harvested from the glass substrate after being poked by the needle. The needle was installed on a x-y-z translation stage, observed under a good quality optical microscope and moved gently close to the micro-structures to detach them from the substrate one by one. Then, a few microliters of the NLC were dropped on the substrate where the micro-structures were placed. After mechanically mixing the NLC with the micro-structures, the nematic colloidal dispersion was collected with a pipette and introduced into a planar cell by capillary forces. The cell was made of two parallel optically transparent indium thin oxide (ITO) coated glasses covered by a thin layer of rubbed-polyimide (PI 5291, Brewer Science) to ensure an excellent planar LC orientation. The ITO coating was used in order to increase the absorption of the laser light of the tweezers at the surface of the glasses and locally

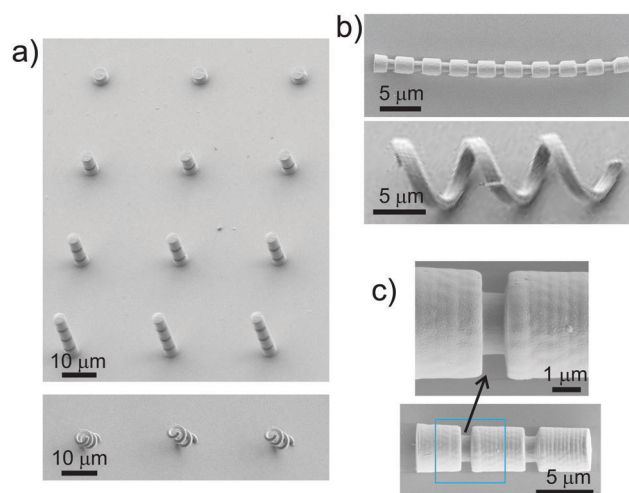


Fig. 1 SEM images of the micro-structures on the glass plate. (a) The polymerized sample is ready to poke the grooved cylinders and helices from the glass plate. (b) Details of the grooved and helical microstructures on the glass after they were poked from the glass. (c) Details of grooved cylinders. Image courtesy of A. Jelen.

melt the LC. The cell gap of 10  $\mu\text{m}$  was controlled with two thin mylar strips and measured by a standard interference technique before filling the colloidal dispersion. In some experiments silica microspheres with a diameter of 4.7  $\mu\text{m}$ , also treated with silane for perpendicular surface anchoring of the NLC, were introduced in the same cell and served as a reference.

We have used laser tweezers with an infrared laser operating at 1064 nm as a light source. The tweezers setup was built around an inverted microscope (Nikon Eclipse, TE2000-U) with a Pixelink PLA 741 camera or a Canon EOS 550D camera at different frame rates from 10 fps to 100 fps. A pair of acousto-optic deflectors driven by a computerized system (Aresis, Tweez 70) was used for trap manipulation.

### 3 Disclination loops around spiral colloids

In this experiment we study topological defects around spiral colloidal particles with homeotropic surface anchoring in a nematic planar cell. After the colloids were dispersed in the NLC and introduced into the measuring cell, the region around the spiral colloid is locally heated into the isotropic phase with a focused laser beam so that one can see the shape clearly in Fig. 2(a), first panel. By shutting off the light the isotropic island undergoes a rapid phase transition that leaves behind a

dense tangle of topological defects. In a fraction of a second this tangle annihilates and pins the defect loops on the helix (Fig. 2 and ESI,† Movie 1).

Two different forms of defect loops can be created around the micro-helix, which are either a small loop in the regions parallel to the rubbing direction (shown with a dotted blue circle in Fig. 2(b)) or an elongated loop in the sections of the helix that make an angle with the rubbing direction (shown with a dotted red circle in Fig. 2(b)). The defect loops are very close to the micro-helix and can be hardly seen. Therefore, a small isotropic region is created in the vicinity of the helix using the laser tweezers. By carefully moving the optically induced isotropic island towards the helix, one can grab the loops and move away from the helix as shown in Fig. 2(c). Fig. 2(c), right panel, shows the schematic representation of the defect rings around the helix. More details can be seen from the ESI,† Movie 1, showing how defects are produced on the helix after quenching the NLC with the laser tweezers. ESI,† Movie 2, shows how individual defects can be grabbed and pulled by the light of the laser tweezers.

The significance of the spiral colloidal particles is their ability to stabilise the plurality of defect rings and prevent their annihilation. Therefore, several defects can be created and they coexist in a very small region of the helix. In the case of a straight micro-rod, which was studied recently,<sup>17</sup> the minimum separation between two defect rings of opposite topological

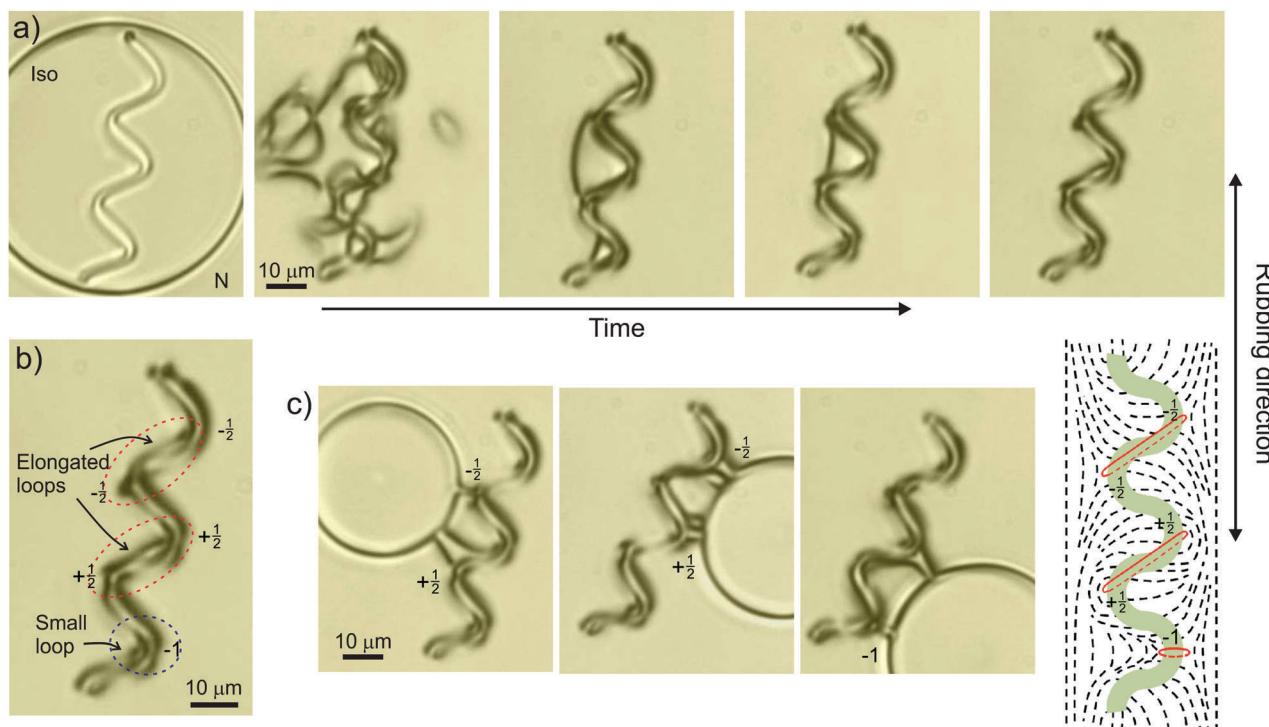


**Fig. 2** Spiral colloidal particles in a nematic planar cell. (a) Creation of a pair of topological defects around the micro-helix by quenching the NLC surrounding the helix using the laser tweezers. Details of quenching can be seen in the ESI,† Movie 1. (b) The red circles show elongated defect loops at an angle of  $\sim 45^\circ$  to the rubbing direction and the blue circle shows a small loop perpendicular to the rubbing direction. (c) The laser tweezers are used to pull the defects away from the helix. Grabbing and tweezing of topological defects can be seen in the ESI,† Movie 2. The last panel shows the schematic representation of the director and loops/defects wrapping the helical particles.

charge and winding is  $\approx 40 \mu\text{m}$ . If defects are closer to each other, the defects attract each other *via* the elastic forces and annihilate. So in order to create two stable defect rings, the length of the micro-rod should be more than  $50 \mu\text{m}$ , and for a large number of defect rings a bigger rod is required. But the wavelike 3D shape of the spiral traps the defects, stabilises them on the helix, and thus prevents them from moving close to each other and annihilation. The spiral shape therefore acts as a series of energy barriers, which are of elastic origin and spatially separate individual defects. If they move closer to each other by thermal motion, the elastic barrier provided by the spiralling shape prevents their further approach and annihilation. On the other hand, as many defects are created in a short part of the helix, it is difficult to determine the topological signature of the defects.

The origin of these elastic energy barriers, which prevent the movement of topological defects along the helices can be understood using a simple model with one  $1/2$  ring on a helical rod, which is placed in a planar nematic cell of thickness  $d$ . It is well known that  $1/2$  defect rings are most stable on a straight fiber, which is directed along the nematic director in a homogeneous nematic cell with planar surface anchoring. The minimum free energy of such a ring is in the situation, when the plane of the ring is perpendicular to the director. Now, if we consider a wavy spiral-like fibre, all sections of this spiral are tilted at an angle  $\alpha$  with respect to the far field director. This means that a  $1/2$  ring shall be free to move along the spiralling fibre, if the spiral is immersed into a NLC with infinite thickness. However, the helices are always placed in

cells with finite thickness of the nematic LC. As a consequence, there will be an energy difference for the  $1/2$  defect ring, which is placed in different sections of the spiral. In those places, where the spiral is in the center of the cell, the elastic energy of the  $1/2$  defect shall be lower than in sections of the spiral, which are closer to the confining surfaces. Close to the surface, the  $1/2$  defect shall be additionally distorted because of the strong and homogeneous anchoring conditions at the surface. We therefore conclude that the confinement of the spiralling fibres in planar cells induces energy barriers for rings placed in different sections of  $1/2$  rings on a spiral. The exact values of these barriers depend strongly on the severity of confinement and can be calculated accurately only by using numerical Landau de Gennes simulations.

We should note that after each quenching the LC around the micro-helix by laser tweezers, a different set of the disclination defects usually appeared, which illustrates the randomness of the selection of possible topological states on a helix. This is easily recognised by comparing two different topologies of the helical particles, presented in Fig. 3(a and b). Although it seems difficult to recognize the type and shape of topological defects, a combination of laser tweezing red-plate visualisation and the use of probe dipolar colloidal particles helps us to determine the type of defect without ambiguity. We have used two methods to determine the presence and the sign of each defect. The sample is placed between crossed polarisers with a  $\lambda$  red wave-plate, which is inserted at 45 degrees angle with respect to the polariser. The colours of the nematic structure around the micro-helix indicate different orientations of the NLC molecules.

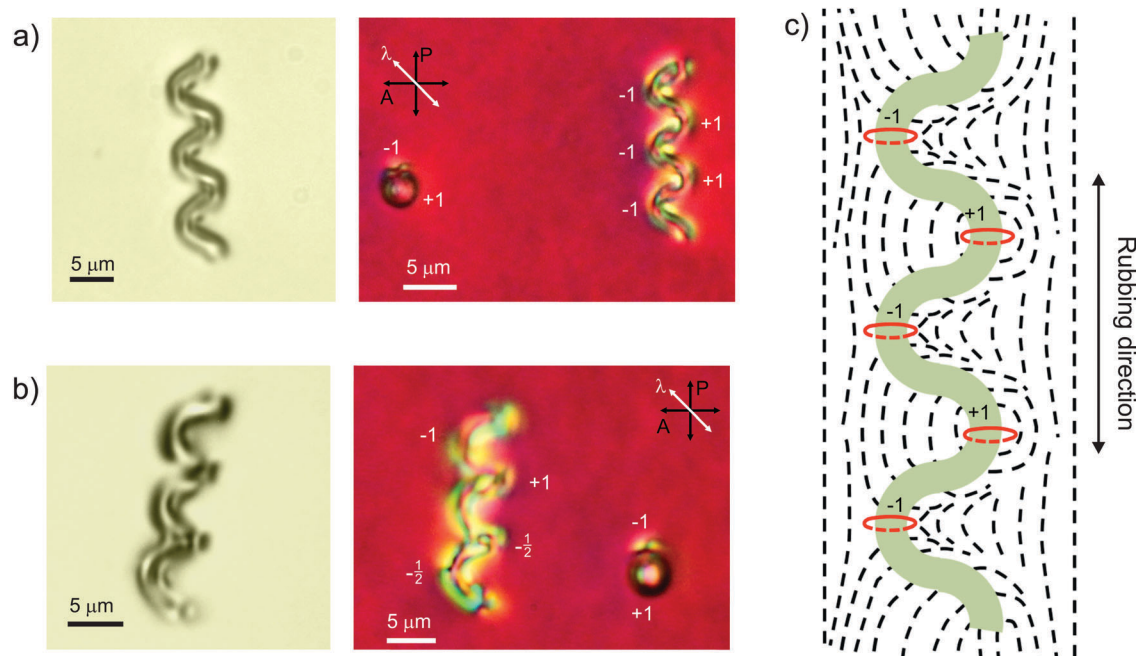


**Fig. 3** (a) Micro-helix with the pairs of topological defects, and a dipolar microsphere, which serves as a reference particle. The second panel is taken under crossed polarisers with inserted  $\lambda$  red wave-plate. By comparing the colours in the vicinity of the micro-helix and a dipolar micro-sphere, one can recognize the sign of the defect rings around the helix in different regions. (b) Another micro-helix with a different set of topological defect loops. The second panel is taken under crossed polarisers with inserted  $\lambda$  red wave-plate. (c) Schematic drawing of the director around the Saturn-rings and Saturn anti-rings on the micro-helix shown in (a).

The color change in each point indicates the existence of the disclination loops. The sign or winding of the disclination loops can be determined by comparing the director pattern in the vicinity of the micro-helix with the corresponding pattern around a dipolar micro-sphere as shown in Fig. 3(a). In this case, the bluish and yellowish colours are clearly visible and indicate two perpendicular directions, inclined at an angle of  $\sim 45^\circ$  with respect to the far-field director. The director pattern around the helix for this experiment is shown schematically in Fig. 3(c).

In some experiments, such as the one shown in Fig. 3(a and b), it is difficult to recognize the colour change around the helix, because of the different combinations of topological defects and the wavelike shape of the helix, so another method has been used to recognize the topological charge of defects, as explained in Fig. 4. This method, also called “a colloidal probe” method is based on a small dipolar colloidal particle (*i.e.* the probe), which is placed close to the defect to be analysed and released. It has been shown consistently in a number of articles<sup>17,26,27</sup> that such a colloidal probe is attracted with its hyperbolic hedgehog (*i.e.* the  $-1$  charged part) to the  $+$  hedgehog and *vice versa*, the  $+1$  part of the probe is always to the  $-1$  hedgehogs or even negatively charged sections of closed loops. We should note that this was demonstrated for topological defects in a form of hedgehogs and loops on a straight fibre.

In the experiment presented in Fig. 4(a), five regions of the micro-helix are marked with ellipsoids to explain the presence of defects, region by region. A small dipolar micro-sphere is left free close to the micro-helix in different positions by the laser tweezers. As the micro-sphere is by convention assigned a  $+1$  topological charge for the particle and  $-1$  topological charge for the accompanying hyperbolic point defect, such a particle induces an elastic distortion that would be repelled by the equally charged part of the disclination line on the micro-helix and attracted to the oppositely charged part. It should be noted that in some nematic textures<sup>11</sup> and around topologically non-trivial objects, such as a torus, the assignment of the topological charge to a particular defect might be ambiguous.<sup>15</sup> For example, it has been demonstrated that a hyperbolic hedgehog can in some cases be assigned either a positive or negative charge. On the other hand, we have performed many experiments and analyses of defects on fibers,<sup>17,26,27</sup> where the charge assignment was not ambiguous and the hyperbolic hedgehog could always and consistently be assigned the  $-1$  charge.

The first panel in Fig. 4(b) shows the micro-sphere with the hyperbolic ( $-1$ ) point defect on top, which is left free in the right side of the micro-helix. First, the dipole started to move upward and then to the micro-helix. From the last panel of Fig. 4(b), one can see that when the dipole approached the helix, the  $-$  end of the dipole was attracted to region 4 and its  $+$  end was attracted to region 2. The regions on the helix and their numbering are shown in Fig. 4(a). Therefore, we expect the  $+$  charged ring in region 4 and the  $-$  charged ring in region 2 of the helix. When the initial position of the dipole was changed and it was released in front of the upper end of the helix, as shown in Fig. 4(c), first panel, the dipole moved through a

diagonal pass and reached the helix similar to the previous experiment (see Fig. 4(c), last panel).

In the following we reversed the direction of the topological dipole and repeated the experiments. Fig. 4(d) and (e), first panels, show the dipole with the hyperbolic hedgehog defect now pointing downwards on the right-hand side of the helix in two different initial positions. In both cases the dipole was attracted to region 2 of the helix with the  $+$  end (*i.e.* the microsphere). Enlarged panels in Fig. 4(c) and Fig. 4(d) clearly show the difference between the dipoles pointing upwards or downwards, and they are fully consistent with the sign allocation shown schematically (Fig. 4(m)). These two experiments clearly confirm the negative sign of region 2.

In the last three experiments the dipole with hyperbolic hedgehog defects pointing upwards was released on the left side of the helix with different initial positions (see Fig. 4(f–h), first panels). Fig. 4(f) shows the dipole moving towards the helix and then downward approaching region 1 with its  $+$  end. Thus, region 1 can be assigned the negative sign. In Fig. 4(g) the initial position of the dipole is lower than in the previous experiment and it is in front of region 1. In this case first, the dipole moved parallel to the helix, then, perpendicular to the helix. The last panel confirmed the negative sign for region 1. As the sign of regions 1 and 2 were the same and negative, we conclude that this is a single elongated ring with  $-1$  topological charge. This is due to topological rules on the fibre,<sup>17</sup> which state that two neighbouring topological defects on a fibre must have opposite winding and sign of the charge. Thereby, if the two regions 1 and 2 show the same sign, they belong to the same topological defect. When the dipole was released in the upper end of the helix, it has been attracted to region 5 from the  $+$  end, which represents negative sign of the disclination defect in this region as shown in Fig. 4(h). From these experiments we can draw the director pattern for this helix, which is shown schematically in Fig. 4(m).

We should point out that there are several studies showing the interaction of micro-spheres with curved walls,<sup>29,30</sup> which is due to the convex and concave surfaces of the micro-spheres and the walls. They have demonstrated lock-and-key interactions, in which a micro-sphere (the key) was attracted to a dale (the lock) along the wavy wall in order to minimize elastic distortion in the nematic director field. The question that appears in our experiment is if the curved shape of the spiral colloidal particles has an effect on the colloidal probe method.

To answer this question we can compare the enlarged images in Fig. 4(c and d). In Fig. 4(c) the  $-1$  hedgehog of the probe is attracted to the  $+1$  hedgehog in Section 4, but at the same time the curved surface of the probe fits nicely the concave section (the dale) of the spiral. This leaves an open question of which mechanism is dominant here: key-lock or pair hedgehog interaction. The answer is shown in the last, enlarged image in Fig. 4(j), where the  $+1$  part of the probe is attracted to the “hill” of the spiral instead of to the dale. This means that in our case the hedgehog–hedgehog interaction is stronger than the key–lock interaction and the convex surface of the sphere fits to the convex surface of the helix because the hedgehog pair

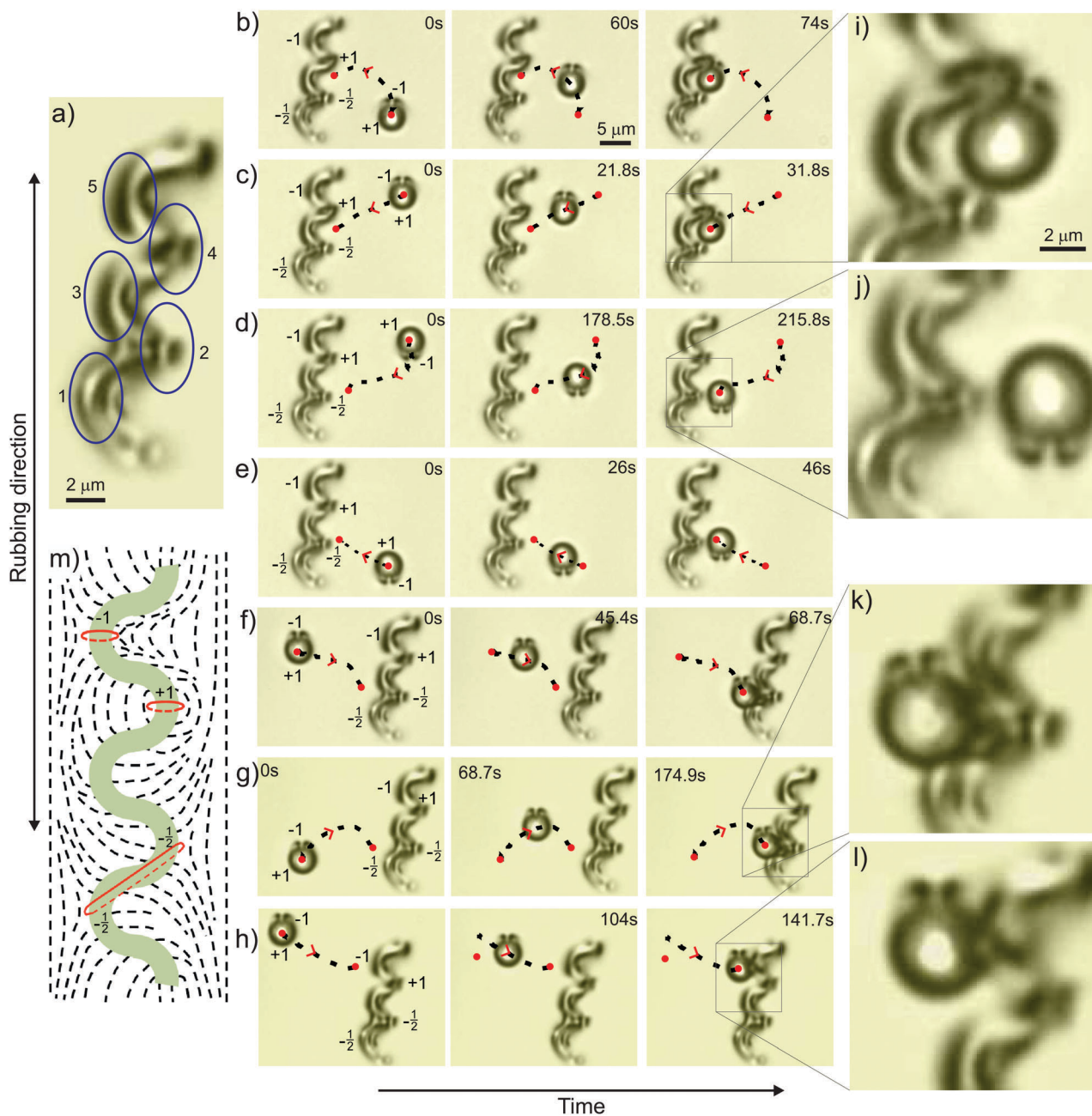


**Fig. 4** (a) Division of the micro-helix with the complex set of topological defect loops in five regions to determine the disclination defects in each region. (b and c) The dipole with the hyperbolic hedgehog defect pointing upward in the right side of the helix is attracted to region 2 from + end and region 4 from its – end. This attraction indicates the – sign for region 2 and the + sign for region 4. (d and e) The dipolar micro-sphere with point defects downward is attracted from the + end to region 2, which demonstrate the – sign for this region. (f and g) Dipole with point defects on top in the left side of the micro-helix has been attracted to region 1 from its + end, assigning this region with the negative sign. (h) Dipole with point defects pointing upward in the left side of the micro-helix is attracted to region 5 from its + end. Thus, the sign of the disclination defect in this region is negative. The dashed lines present the trajectory of the dipole. (i–l) Show higher magnification details of the interaction between the micro-sphere and the defect rings on the helix. (m) Schematic presentation of the director pattern around the micro-helix.

interaction is stronger and decisive. This is also evident by comparing Fig. 4(k) and (l), which also gives a consistent answer. The colloidal probe method therefore gives consistent assignment of the sign of the topological charge also on wavy, spiral colloidal particles.

To this end and to be absolutely sure we have also performed other experiments using helical particles with longer

pitch and smaller micro-sphere, which should change the key-lock interaction but not the pair hedgehog interaction. The pitch of the helix was increased to  $16\ \mu\text{m}$  and the sphere diameter was decreased to  $2.4\ \mu\text{m}$ . The cell gap was  $12\ \mu\text{m}$ . In this experiment shown in Fig. 5 the dipole with hyperbolic hedgehog defects pointing upwards was released on the right side of the helix. First, the dipole is attracted to a ring on the

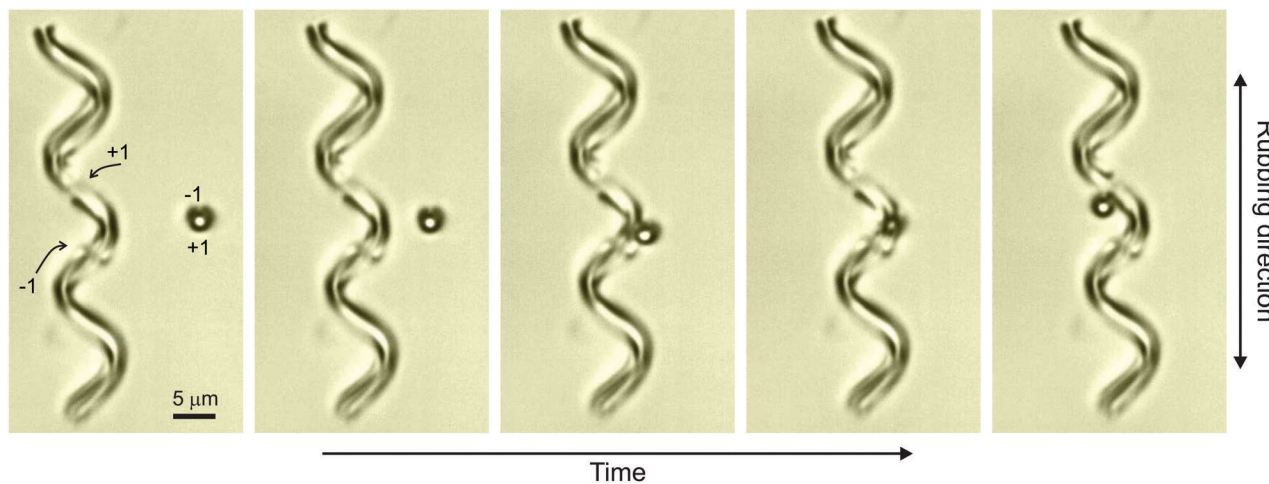


Fig. 5 The interaction between topological defect rings on the helix and dipolar micro-sphere. The sphere is attracted to a ring on the helix from its + end, then passes through the helix and interacts with another ring from its – end (point defect). The video of this experiment can be seen in the ESI,† Movie 3.

helix from its + end and then passes through the helix and interacts with another ring from its – end (see Fig. 5). The micro-sphere practically does not see the wavy shape of the helix and is directly attracted to the hedgehogs on a spiral. This confirms our conjecture that oppositely charged defects are attracted to each other, the sign of the defect rings can be determined unambiguously also on spiral colloidal particles.

## 4 Topological charges on a micro-grooved cylinder

Micro-grooved-cylinders are fabricated with DLW as explained in Section 2. The micro-grooved-cylinders with a diameter of 2  $\mu\text{m}$  and normal surface anchoring are inserted into the planar nematic cell. Several defect rings are created very close to each other and are stable for a very long time as shown in Fig. 6(a). This is due to the grooved surface of the cylinder, which prevents the motion of the defect rings once they are created. One can clearly see from the crossed polariser image in the second panel of Fig. 6(a) that the defects are trapped into the grooves of the rod, which is also visible from the red-plate image in the far right panel of Fig. 6(a).

In this case the defects were created during the flow of nematic dispersion into the measuring cell. The topological defects which are formed while filling the sandwich cell are spontaneous and uncontrolled. However, we can create them also by using the laser tweezers. The controlled creation and manipulation of topological defects using the laser tweezers are shown in Fig. 6(b). The second panel of Fig. 6(b) shows how the ring, which is trapped in one of the grooves, is grabbed with the laser tweezers and dragged up. That leaves enough space below the rings to create another pair using laser tweezers, as shown in the sequence of images in Fig. 6(c).

Because of the topological rules on a long fibre, the sign of topological charge of neighbouring defects is always opposite,

which results in alternating charge of defects, as we move along the fibre. Because of opposite charge, any pair of defects on a fibre is attracted to each other and tries to annihilate and lower the total free energy of the system. If grooves are made into the fibre, they prevent the motion of topological defects and stabilize oppositely charged defect pairs. However, if the separation between the grooves is made smaller, there shall be a critical separation, where the elastic attractive forces shall become stronger than the stabilizing force due to grooves and the pair shall be released from the grooves and will annihilate. To estimate the minimum separation between the grooves that could stabilise oppositely charged defects, we need to measure the attractive force between oppositely charged topological defects as a function of their separation.

The elastic attractive force between two oppositely charged defect rings was measured in a separate experiment, which is illustrated in Fig. 7. We took a small rod with a diameter of 2  $\mu\text{m}$  and created a pair of oppositely charged rings by using the laser tweezers, as described previously.<sup>17</sup> The two rings are attracted to each other because of the elastic deformation of the director field, and they start approaching each other and finally annihilate into the vacuum, as illustrated by a series of video snapshots in Fig. 7(a). The attractive force between the two defect rings can be calculated from the captured video following the well-known procedure.<sup>33</sup> First, we determine instantaneous positions of each ring for each captured frame by tracking their positions. Then we calculate their instantaneous velocities by numerical differentiation of their trajectories. Once we know the velocities of both rings, we can calculate the attractive force  $F_{\text{attract}}$  between them. Namely, the motion of a defect ring can be considered as a motion of a line-like object through a viscous fluid. The Stokes drag force on such a closed line of length  $L$  is given by  $F_{\text{drag}} = \pi R L v$ . Here,  $R$  is the viscous drag coefficient per unit length of the line and  $v$  is the velocity of the line. Viscous drag coefficient  $R$  has been measured for 1/2 disclination lines in 5CB by Mertelj *et al.*<sup>31</sup> and is  $R = 0.15 \text{ Pa s}$ .

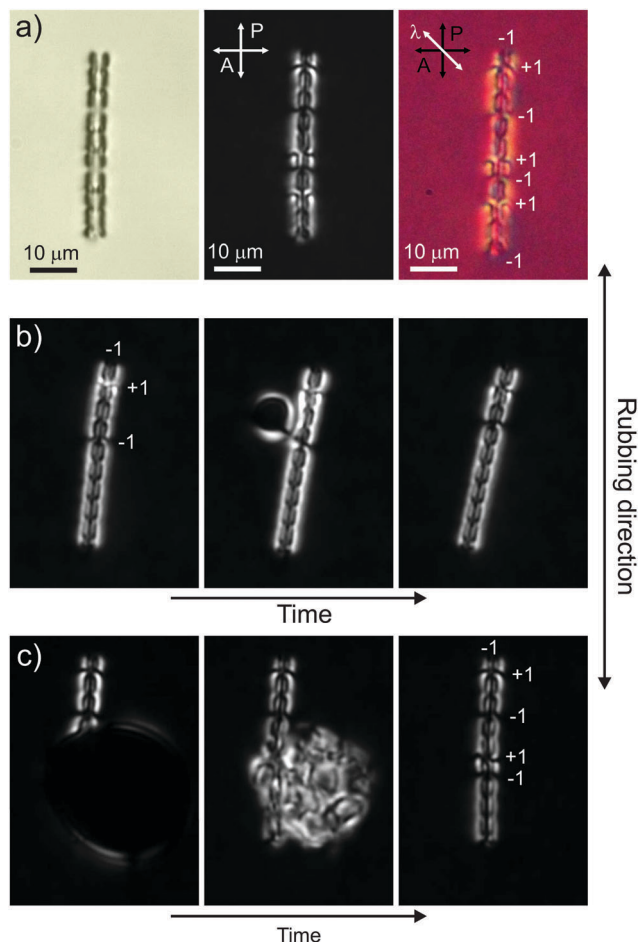


**Fig. 6** Defects on a micro-grooved cylinder in a planar nematic cell. (a) The left image presents the unpolarised optical micrograph of a grooved cylinder which is accompanied by a Saturn-ring and three extra pairs of defects, which are created during the filling of the measurement cell by the nematic dispersion or using the laser tweezers. Note the different brightness of the structures in the grooves, which corresponds to opposite charge and winding of defect rings. The middle image is taken under crossed polarisers, with notable differences in the brightness of different grooves. The right panel is taken under crossed polarisers with a full wave-plate, which is inserted at 45 degrees with respect to the polariser P and crossed analyser A. The blue and yellow colors clearly show the reversed director field in the vicinity of the grooved cylinder, which indicates alternation of loops' windings and charge. (b) Laser tweezers are used to move a Saturn-ring along the grooved cylinder. (c) A pair of topological defects are created using the light of laser tweezers. Note an odd number of defects on a grooved cylinder in all cases.

$L$  is in our case the diameter of the defect ring which is equal to  $3.2 \mu\text{m}$ . The motion of defect lines in LCs is overdamped, which means that their acceleration is negligible and the sum of all forces on a moving ring is zero,  $F_{\text{drag}} + F_{\text{attract}} = 0$ . Because we know the Stokes drag force from our experiments, we can determine the elastic attractive force between the oppositely charged rings on a fibre, which is shown in Fig. 7(b). At large separation,  $\sim 6 \mu\text{m}$ , the force is  $\sim 4 \text{ pN}$  and sharply increases to  $\sim 15 \text{ pN}$  at a separation of  $\sim 2.6 \mu\text{m}$  as shown in Fig. 7(b). For shorter separation the rings join together, create a single neutral ring, and then annihilate into the vacuum.

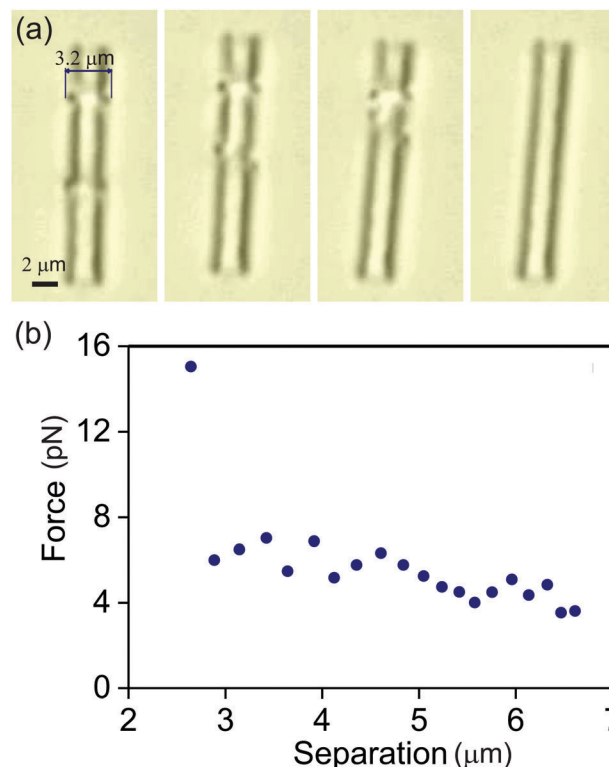


**Fig. 7** (a) Pair interaction of defect rings freely moving on a cylinder with a diameter of  $2 \mu\text{m}$ . (b) The attractive force between two defect rings, as determined by video tracking of particles.<sup>33</sup>

On the other hand, the two rings have to be pulled-out of the grooves if they are to move towards each other. This means that force is required to stretch the loop to move it out of the grooves and this force can be provided only by the attractive elastic force between the rings. We can estimate the force needed to stretch the rings from the experiments of colloidal entanglement by Ravnik *et al.*<sup>32</sup> It was measured by the laser tweezers that a typical magnitude of the force needed to stretch and elongate the  $-1/2$  Saturn ring in 5CB is around  $\sim 30 \text{ pN}$ . This means that the attractive elastic force between the oppositely charged rings is not strong enough to move the defects from the grooves at the smallest separation which was measured in our experiment in Fig. 7(b), *i.e.*  $\sim 2.6 \mu\text{m}$ . This is therefore the upper estimated value for the critical separation between the  $-1/2$  and  $+1/2$  rings on grooved rods, where the defects are still stable. The exact value of the smallest separation at which the rings on a grooved rod are still stable can only be calculated numerically using fully tensorial Landau-de Gennes modelling. However, it is clear from our estimate that grooves on a rod are extremely effective in stabilizing the defects on a fibre, presumably down to micrometer separation.

The experiments show that a grooved cylinder with 2 grooves and 3 ribs ( $R = 3$ ) can carry either 1 or 3 topological defects, as illustrated in Fig. 8. A single topological defect is in the form of hyperbolic hedgehog or a Saturn-ring as shown in Fig. 8(b). 3 topological defects exist in the form of one point defect with a topological charge of  $-1$ , one Saturn-anti-ring with a charge

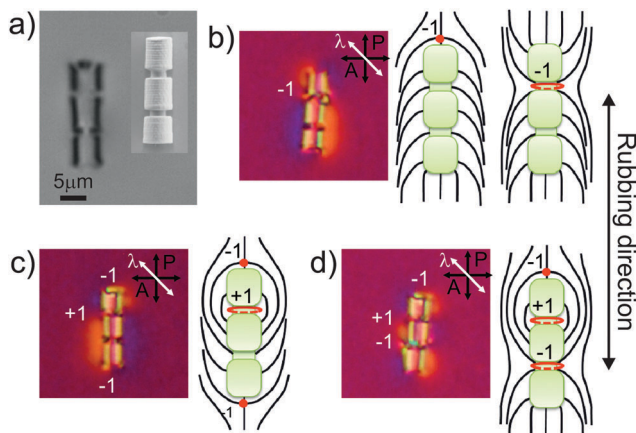


**Fig. 8** Micro-grooved cylinder with 2 grooves. (a) The unpolarised optical micrographs of a grooved cylinder. Note a difference in the apparent brightness of two grooves. This is because one of the grooves is filled with a  $-1$  defect and the other is not. The SEM image before inserting the particle in LC is shown in the inset. (b) Optical micrograph of a grooved cylinder accompanied by a Saturn-ring, first panel. The second and third panels show schematically the director field arising from two possible kinds of topological defects, which are either a point or ring defect, respectively. (c) Another possible constellation of unit charge defects on a cylinder with two grooves: one Saturn-anti-ring with  $+1$  charge is accompanied by two hyperbolic hedgehogs on each end of the cylinder. (d) The last constellation is made of one pair of Saturn ring and anti-Saturn-ring, and a hyperbolic hedgehog on one end of the cylinder. (b–d) The micrographs are taken under crossed polarisers with an inserted optical red retardation plate.

of  $+1$  and the third one can be either a hyperbolic point defect (Fig. 8(c)) or a Saturn-ring (Fig. 8(d)) with a charge of  $-1$ . In all cases we have an odd number of defects and their charge adds up to  $-1$ .

Fig. 9 represents schematically the relation between  $R$  and the number of topological defects for various types of grooved cylinders. The number of ribs  $R$  controls the number of maximum topological defects that can be efficiently stabilised on the particle. If  $R$  is an odd number, the maximum number of topological defects is equal to  $R$ . If  $R$  is an even number, the maximum number of topological defects is equal to  $R + 1$ . Regardless of the number of ribs/grooves, the total number of topological defects on any kind of rod is always an odd number. The grooved cylinder itself can be assigned a  $+1$  charge and this charge has to be compensated by the accompanying defect(s). To satisfy the conservation of the total topological charge any even number of topological defects can therefore also be created and stabilised by using the laser tweezers.

Fig. 9(a) shows a cylinder with  $R = 2$  and a single groove. The maximum number of topological defects is equal to 3. A cylinder with  $R = 3$  and 2 grooves is also accompanied by 3 topological defects (Fig. 9(b)) as discussed in detail in Fig. 5. A cylinder with  $R = 4$  can carry either 3 or 5 topological defects as shown in Fig. 9(c). Let us note that defects could be re-located to different grooves, as far as their total charge equals to  $-1$ . The Saturn-anti-ring in Fig. 9(c), first panel, is located in the groove between two upper ribs, but can be moved between two other ribs using laser tweezers. A cylinder with

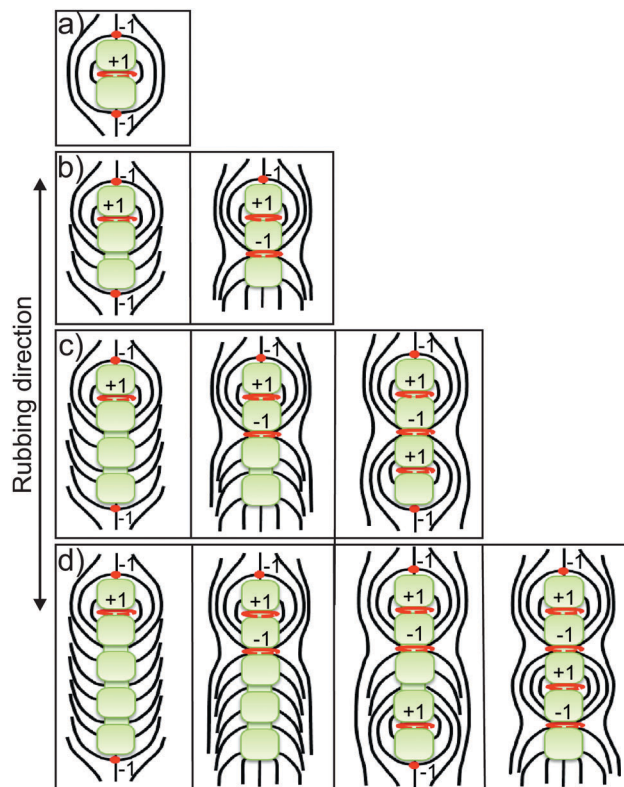


**Fig. 9** Schematic representation of topological states stabilised by micro-grooved cylinders. (a–d) Defects on a rod are of unit charge and appear in the form of a hyperbolic hedgehog, Saturn-ring or Saturn-anti-ring. The maximum number of defects is controlled by the number of ribs/grooves.

$R = 5$  is accompanied by 3 or 5 topological defects (see Fig. 9(d)). Two first panels show the cylinder with 3 topological defects, which are in the form of two hyperbolic hedgehogs and one Saturn-anti-ring (first panel) or one hedgehog hyperbolic, one Saturn-anti-ring, and one Saturn-ring (second panel). Two last panels show the cylinder with 5 topological defects, which are in the form of two hyperbolic hedgehogs, two Saturn-anti-rings and one Saturn-ring (third panel) or one hedgehog hyperbolic, two Saturn-anti-rings and two Saturn-rings (fourth panel). In all the grooved cylinders in Fig. 9, the hyperbolic hedgehogs are located in the end of the cylinder and the Saturn-rings and Saturn-anti-rings are located in the grooves between the ribs alternatively. Note the alternation of the sign of neighbouring defects, which is a common topological rule for charges on a rod.<sup>17</sup>

## 5 Interaction between micro-grooved cylinders

When several grooved cylinders are brought together in the nematic liquid crystal, they start to interact with each other and their regions of distortion start to overlap. An arbitrary number of topological defects and their random positions on the particles enable the design of quite complex anisotropic building blocks. These particles are smart which means that they are capable of recognising topological defects with plus or minus

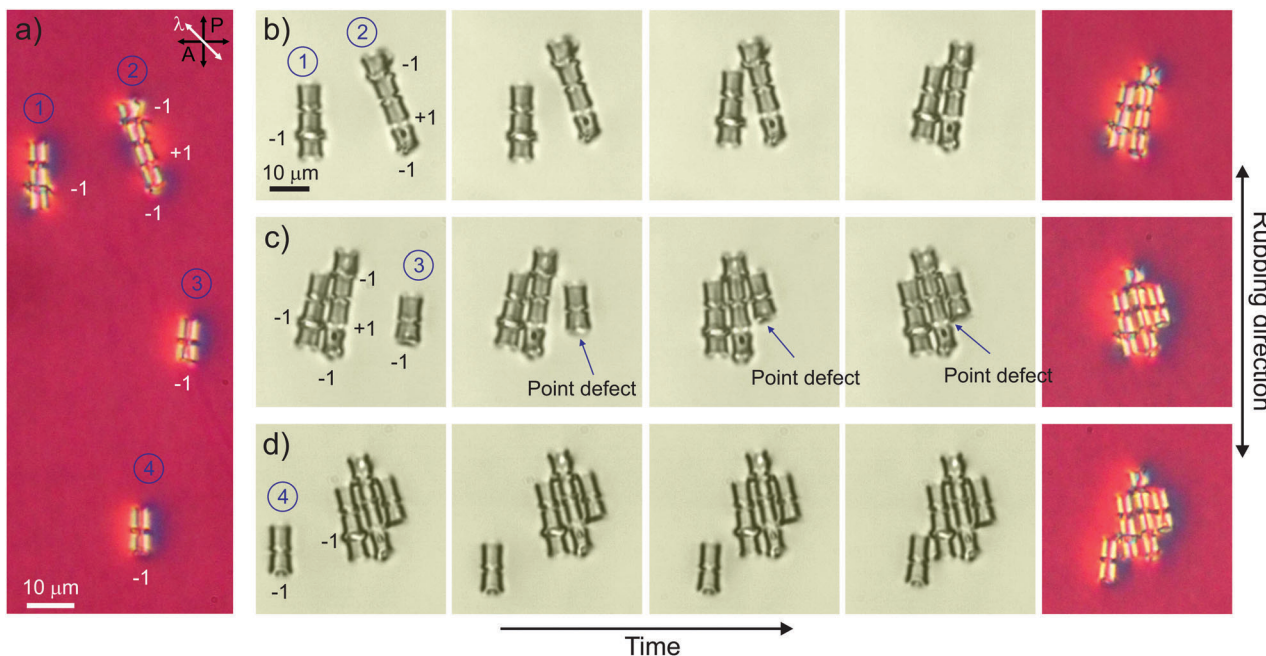


**Fig. 10** Entangled grooved cylinders with an arbitrary number of grooves and defects. (a) Grooved cylinders viewed between crossed polarisers and red plate added at 45 degrees angle. (b) Video frames showing the interaction of particle 1 with  $R = 3$  and a single defect and particle 2 with  $R = 4$  and three topological defects: one anti-defect and two defects. The + end of particle 1 is attracted to the defect on particle 2 such that the defect on particle 1 is entangled to the anti-defect on particle 2 resulting in the formation of a colloidal dimer. (c) Particle 3 with  $R = 2$  and a single defect released from the optical trap next to particle 2 is attracted to the defect on particle 2 from its + end. The defect on particle 3 is moved towards the anti-defect on particle 2, as shown with blue arrows. (d) Another particle with  $R = 2$  and a single defect is released from the laser trap next to particle 1. This particle travels a long way downward, thereby minimizing the elastic energy of the system. The + end of particle 4 is attracted to the defect on particle 1 and a colloidal tetramer is created.

charges *via* a simple universal law: equally charged defects repel from each other and oppositely charged defects are attracted to each other.

Fig. 10(a) shows four grooved cylinders with various numbers of ribs/grooves and topological defects and their interactions, which results in complex structures, engineered by the topology. First, two grooved cylinders with  $R = 3$  and  $R = 4$  (marked with numbers 1 and 2, respectively) are left free in the vicinity of each other. Particle 1 has one defect with  $-1$  charge and particle 2 has two defects with  $-1$  charges and one defect with  $+1$  charge. Fig. 10(b) shows the sequence of optical micrographs of the attraction between these two particles, which are extracted from the recorded video. During this interaction, particle 1 moves downward to position its + end toward the  $-1$  ring on particle 2, while the  $-1$  ring on particle 1 is bound to the  $+1$  ring on particle 2. The last panel shows the configuration of the director field around the colloidal dimer using the  $\lambda$  wave-plate. Particle 3 with a hyperbolic hedgehog defect pointing downwards is brought close to the colloidal dimer by the laser tweezers and left free by switching off the laser (Fig. 10(c)). Particle 3 is attracted to the  $-1$  ring on particle 2 from its + end. The  $-1$  point defect on particle 3 starts to move towards the  $+1$  ring on particle 2 as shown in Fig. 10(c), second to fourth panels. Fig. 10(d) shows the interaction between the colloidal trimer and particle 4 with  $R = 2$  and a hyperbolic hedgehog defect. One can see from the sequence of

optical micro-graphs that particle 4 starts to move downward and then to the colloidal trimer in order to match the director field within the colloids and minimize the elastic energy. The + end of particle 4 is attracted to the  $-1$  ring on particle 1.

## 6 Conclusions

This work demonstrates that a complex topology can be realised on a simple object with genus  $g = 0$ . The realisation of complex topological states is made possible by geometric shaping of rods/cylinders, which acts as a stabilising factor preventing defect annihilation. This shaping can be done either by twisting a rod into a helix or by making grooves in the rod. Both ways we introduce an energy barrier between neighbouring and oppositely charged topological defects, which prevents their movement and subsequent annihilation. The twisting or grooving topologically simple objects thereby provides a new method for producing complex and reconfigurable topological states. Our results indicate that by producing grooves on fibres one could stabilize topological defects on presumably close to a micrometer separation. Such a fibre could therefore carry a huge number of oppositely charged defects, which could have interesting consequences for colloidal interactions. From the fundamental aspect, this work fully supports the Gauss–Bonnet theorem,<sup>33</sup> stating that the total topological charge of all

hedgehog defects on an object should be equal to  $g - 1$ , where  $g$  is the genus of the particle.

## Conflicts of interest

There are no conflicts to declare.

## Acknowledgements

This work was supported by the European Commission Marie Curie project HIERARCHY grant PITN-GA-2008-215851 (M. N.) and the Slovenian Research Agency (ARRS) contracts P1-0099 and J1-6723 (I. M.).

## References

- M. Kléman, *Points, Lines and Walls: In Liquid Crystals, Magnetic Systems and Various Ordered Media*, Wiley, Chichester, 1983.
- P. G. de Gennes and J. Prost, *The Physics of Liquid Crystals*, Oxford University Press, Oxford, 2nd edn, 1993.
- M. Kléman and O. D. Lavrentovich, *Soft Matter Physics: An Introduction*, Springer-Verlag, New York, 2003.
- N. Mermin, *Rev. Mod. Phys.*, 1979, **51**, 591–648.
- H.-R. Trebin, *Adv. Phys.*, 1982, **31**, 195–254.
- R. Mosseri, *C. R. Chim.*, 2008, **11**, 191–197.
- M. V. Kurik and O. D. Lavrentovich, *Sov. Phys. – Usp.*, 1988, **31**, 196–224.
- S. Chandrasekhar and G. Ranganath, *Adv. Phys.*, 1986, **35**, 507–596.
- I. Chuang, R. Durrer, N. Turok and B. Yurke, *Science*, 1991, **251**, 1336–1342.
- M. J. Bowick, L. Chandar, E. A. Schiff and A. M. Sivasava, *Science*, 1994, **263**, 943–945.
- G. P. Alexander, B. G. Chen, E. A. Matsumoto and R. D. Kamien, *Rev. Mod. Phys.*, 2012, **84**, 497–514.
- M. A. Gharbi, Da. Seč, T. Lopez-Leon, M. Nobili, M. Ravnik, S. Žumer and C. Blanc, *Soft Matter*, 2013, **9**, 6911–6920.
- T. Lopez-Leon and A. Fernandez Nieves, *Colloid Polym. Sci.*, 2011, **289**, 345–359.
- F. Serra, M. Buscaglia and T. Bellini, *Mater. Today*, 2011, **14**, 488–494.
- B. Senyuk, Q. Liu, S. He, R. D. Kamien, R. B. Kusner, T. C. Lubensky and I. I. Smalyukh, *Nature*, 2013, **493**, 200–205.
- B. Senyuk, M. B. Pandey, Q. Liu, M. Tasinkevych and I. I. Smalyukh, *Soft Matter*, 2015, **11**, 8758–8767.
- M. Nikkhou, M. Škarabot, S. Čopar, M. Ravnik, S. Žumer and I. Mušević, *Nat. Phys.*, 2015, **11**, 183–187.
- T. Araki, M. Buscaglia, T. Bellini and H. Tanaka, *Nat. Mater.*, 2011, **10**, 303–309.
- J. Dontabhaktuni, M. Ravnik and S. Žumer, *Soft Matter*, 2012, **8**, 1657–1663.
- U. Tkalec, M. Ravnik, S. Čopar, S. Žumer and I. Mušević, *Science*, 2011, **62**, 333.
- H. Stark, *Phys. Rep.*, 2001, **351**, 387–474.
- I. Mušević and M. Škarabot, *Soft Matter*, 2008, **4**, 195–199.
- U. Tkalec, M. Škarabot and I. Mušević, *Soft Matter*, 2008, **4**, 2402–2409.
- S. M. Hashemi, U. Jagodič, M. R. Mozaffari, M. R. Ejtehad, I. Mušević and M. Ravnik, *Nat. Commun.*, 2017, **8**, 14026.
- Y. Yuan, A. Martinez, B. Senyuk, M. Tasinkevych and I. I. Smalyukh, *Nat. Mater.*, 2018, **17**, 71–80.
- M. Nikkhou, M. Škarabot and I. Mušević, *Phys. Rev. E*, 2016, **93**, 062703.
- M. Nikkhou, M. Škarabot and I. Mušević, *Eur. Phys. J. E: Soft Matter Biol. Phys.*, 2015, **38**, 23.
- M. Nikkhou, M. Škarabot, S. Čopar and I. Mušević, *Eur. Phys. J. E: Soft Matter Biol. Phys.*, 2016, **39**, 100.
- Y. Luo, F. Serra and K. J. Stebe, *Soft Matter*, 2016, **12**, 6027–6032.
- Y. Luo, D. A. Beller, G. Boniello, F. Serra and K. J. Stebe, *Nat. Commun.*, 2018, **9**, 3841.
- A. Mertelj and M. Čopic, *Eur. Phys. J. E: Soft Matter Biol. Phys.*, 2004, **69**, 021711.
- M. Ravnik, M. Škarabot, S. Žumer, U. Tkalec, I. Poberaj, D. Babič, N. Osterman and I. Mušević, *Phys. Rev. Lett.*, 2007, **99**, 247801.
- I. Mušević, *Liquid Crystal Colloids*, Springer, Cham, 2017.